Applied Catalysis B: Environmental 329 (2023) 122569

Contents lists available at ScienceDirect

Applied Catalysis B: Environmental

journal homepage: www.elsevier.com/locate/apcatb

Switching the reaction mechanisms and pollutant degradation routes through active center size-dependent Fenton-like catalysis

Xinhao Wang [a,d], Zhaokun Xiong [a,b,d,e,*], Hongle Shi [c], Zelin Wu [a,d], Bingkun Huang [a,d], Heng Zhang [a,d], Peng Zhou [a,d], Zhicheng Pan [e], Wen Liu [b], Bo Lai [a,d,e,*]

[a] State Key Laboratory of Hydraulics and Mountain River Engineering, College of Architecture and Environment, Sichuan University, Chengdu 610065, China
[b] The Key Laboratory of Water and Sediment Sciences, Ministry of Education, College of Environmental Sciences and Engineering, Peking University, Beijing 100871, China
[c] Sichuan Academy of Eco-Environmental Sciences, Chengdu 610041, China
[d] Sino-German Centre for Water and Health Research, Sichuan University, Chengdu 610065, China
[e] Water Safety and Water Pollution Control Engineering Technology Research Center in Sichuan Province, Haitian Water Group, China

ARTICLE INFO

Keywords:
Size-dependent catalysis
Single atom catalyst
Reaction mechanism
Degradation routes
Peroxymonosulfate

ABSTRACT

Rationally regulating reaction mechanisms in Fenton-like reactions by tuning the properties of catalysts is of great significance, but still challenging. Herein, we synthesized various active center size-dependent catalysts to realize the switching of reaction mechanisms and pollutant degradation routes in peroxymonosulfate (PMS) activation systems. The results illustrated that the reaction mechanism transformed from radical oxidation (51.64%) to nonradical oxidation (89.92%) with the decrease of active center size from nanoparticle (Co_{NP}-NC) to single atom (Co_{SA}-NC). The evolution of reactive species switched the degradation intermediates and pathway of sulfisoxazole (SIZ). The generation of singlet oxygen ($^1O_2$) in Co_{SA}-NC/PMS tends to selectively attack electron-rich site of SIZ, while reaction between radicals and SIZ prefers non-selective oxidation in Co_{NP}-NC/PMS system. Besides, the toxicity tests indicated that the conversion from non-selective to selective oxidation resulted in lower toxicity of effluent after reaction, which can further reduce environmental risks of effluent.

1. Introduction

Peroxymonosulfate (PMS)-based Fenton-like process is considered a potential strategy for wastewater remediation owing to the generation of various reactive oxygen species (ROS) [1]. The activation of PMS can be initiated via multiple means involving light, heat, ultrasound, electricity, and heterogeneous activation by catalysts [2,3]. Given that, substantial research effort has been devoted to the improvement of PMS activation efficiency, the exploitation of novel heterogeneous catalysts as well as the analysis of activation mechanisms [4,5]. Along with the rapid evolution of catalysts, a growing number of researchers have shifted their interests to complex catalysts for chemical synthesis, activation property development and analysis of deeper activation mechanisms [6,7].

Currently, the generation of ROS for the degradation of contaminants via PMS activation is divided into radical and nonradical pathways [8,9]. Generally, the effectiveness of PMS activation systems on recalcitrant pollutants degradation relies on the strong oxidation of radicals including hydroxyl radicals ($^{\bullet}OH$, $E^0 = 1.8–2.7$ V) and sulfate radicals ($SO_4^{\bullet-}$, $E^0 = 2.5–3.1$ V) [10,11]. Metal ions and metal oxides such as Co, Fe, Mn, Cu, and others have been frequently used for PMS activation systems to advantageously produce radicals [12–14]. Furthermore, once the nonradical oxidation pathway was originally found in Gif chemistry, piles of papers were published on it [15]. The typical nonradical pathway in which contaminants were degraded via direct electron transfer was found in the system of PMS/N-doped carbon nanotubes or PMS/nitrogen coordinated Co single-atom catalyst [8,16]. In addition, N-doped carbonaceous materials can boost the production of singlet oxygen ($^1O_2$) from PMS, which belongs to the typical nonradical species [17,18]. Compared radicals to nonradicals, radical species ($SO_4^{\bullet-}$ and $^{\bullet}OH$) show a strong oxidizing power toward a broad range of pollutants, but nonradical species ($^1O_2$) exhibit a highly selective for the electron-rich contaminants and have a strong resistance to coexisting matters [15,19,20]. Given that, researchers have demonstrated great

* Corresponding authors at: State Key Laboratory of Hydraulics and Mountain River Engineering, College of Architecture and Environment, Sichuan University, Chengdu 610065, China

E-mail addresses: scuxzk@scu.edu.cn (Z. Xiong), laibo@scu.edu.cn (B. Lai).

https://doi.org/10.1016/j.apcatb.2023.122569
Received 4 January 2023; Received in revised form 14 February 2023; Accepted 2 March 2023
Available online 5 March 2023
0926-3373/© 2023 Elsevier B.V. All rights reserved.

interest in the regulation of radical/nonradical mechanisms in PMS activation systems.

Ordinarily, the adoption of porous engineering and doping tactics are widely accepted methods to enhance the performance of catalysts. However, it also reported that modified graphene or loaded CuO/Fe_3O_4 catalysts could switch the radical/nonradical route in the process of PMS activation [21,22]. Besides, it is worth mentioning that the association of active sites to reactive species and organic degradation routes in PMS activation was developed [23]. However, it is significant and challenging to switch the radical/nonradical mechanisms of PMS activation and the degradation route of contaminants through a reaction-target catalyst. Moreover, it is a significant but yet unclear issue to reduce the biotoxicity of effluent through the regulation of ROS and degradation pathway. Collectively, it is vital to investigate the mechanism between the sites of organics attacked and ROS to control the generation of intermediates and regulate the contaminant degradation route as well as biotoxicity of effluent.

Herein, a series of Co-based catalysts with different active center sizes (nanoparticles, metal clusters, and single atoms), denoted as Co_{NP}-NC, Co_{MC}-NC, and Co_{SA}-NC, respectively, were fabricated to active PMS for sulfisoxazole (SIZ) degradation. The catalytic activity of PMS activation by three catalysts for SIZ degradation was examined. The target pollutant SIZ, as an antibiotic, exhibits antibacterial activities and is refractory in an aqueous solution, posing environmental hazards [9]. Hence, the correlation of active center size to reaction mechanism and pollutant degradation routes was explored. Furthermore, the regulation mechanisms of the degradation pathway and toxicity of SIZ and intermediates in the process of PMS activation were deeply analyzed based on ultraperformance liquid chromatography-quadrupole time-of-flight premier mass spectrometry (UPLC-QTOF-MS/MS) and density functional theory (DFT) calculations. This work can provide a theoretical foundation and technical insights for the PMS-based Fenton-like reaction and the results will be beneficial for the development of selective removal of emerging pollutants in wastewater.

2. Materials and methods

2.1. Chemicals

Sulfisoxazole (SIZ, 99%), bisphenol A (BPA, 99%), phenol, peroxymonosulfate (PMS, 0.5 $K_2SO_4 \cdot 0.5KHSO_4 \cdot KHSO_5$), furfuryl alcohol (FFA), 2,2′-azinobis(3-ethylbenzothiazoline −6-sulfonic acid ammonium salt) (ABTS), 5,5-dimethyl-1-pyrroline N-oxide (DMPO), 2,2,6,6-tetramethyl-4-piperidinyloxyl (TEMP), 9,10-diphenylanthraquinone dyes (DPA), benzoic acid (BA), nitrobenzene (NB), β-carotene, methyl phenyl sulfoxide (PMSO), methyl phenyl sulfone ($PMSO_2$), *p*-benzoquinone (*p*-BQ), dimethyl sulfoxide (DMSO), ethylenediaminetetraacetic acid (EDTA), and $CoSO_4 \cdot 7H_2O$ were purchased from Shanghai Aladdin reagent Inc. $Co(NO_3)_2 \cdot 6H_2O$, $Zn(NO_3)_2 \cdot 6H_2O$, 2-methylimidazole (2-MeIM), methanol (MeOH), tert-butyl alcohol (TBA), $Na_2S_2O_3$, H_2SO_4, and NaOH were all purchased from Chengdu Kelong chemical reagent factory. Deionized water was used throughout the whole experiment process.

2.2. Synthesis of catalysts

The preparation of cobalt-based catalyst mainly consists of two steps as shown in Fig. S1 according to the previous works with slight modification [24,25]. The size of the catalyst is controlled by adjusting the content of Zn/Co (called Co_{SA}-NC, Co_{MC}-NC, and Co_{NP}-NC according to the molar ratio of 8:1, 4:1, and 1:1). Firstly, the fixed metal dosage is 3 mM, viz, 2.67 mM $Zn(NO_3)_2 \cdot 6H_2O$ and 0.33 mM $Co(NO_3)_2 \cdot 6H_2O$ (ZnCo = 8:1) is dissolved in 30 mL MeOH (phase A), followed by 12 mM 2-MeIM in 5 mL MeOH (phase B). After completely dissolving phases A and B, the metal salt solution is slowly poured into the (7.5 mL/s) 2-MeIM solution, and the mixed solution is stirred by magnetic force at a rate of 300 r/min. After complete mixing, the rotational speed is modulated by 500–600 r/min for 5 min. Then, the solution will be heated at 120 °C for 4 h in a hydrothermal reactor. After cooling, the supernatant is removed to keep precipitated, followed by four washes and centrifugations with methanol, followed by drying in a vacuum drying box at 70 °C to obtain Zn/Co-precursor.

Secondly, evenly grind the dried Zn/Co-precursor before calcining them in a tube furnace for 2 h with nitrogen filling. The temperature rises from room temperature to 900 °C at the rate of 2.25 °C/min, and remains at 900 °C for 2 h. The flow rate of nitrogen is 150 mL/min. After cooling in the tube furnace, the material was acid-washed for 4 h in a water bath at 80 °C with 1.5 M H_2SO_4, then washed and filtered with a large amount of deionized water, and finally dried in a vacuum drying box at 70 °C to obtain Co_{SA}-NC. Similarly, the NC, Co_{NP}-NC, and Co_{MC}-NC were synthesized according to the same procedures except that the Zn/Co molar ratios were 1:0, 1:1, and 4:1.

2.3. Experimental procedure

All the experiments were carried out in a 250 mL glass beaker containing 100 mL of SIZ (5 mg/L) with a constant stirring rate of 300 rpm at 30 ± 1 °C. Each reaction was started with the required dosages of catalysts and PMS. At each time interval, 0.22 μm polytetrafluoroethylene syringe filter discs were used to filter the samples, which then were quenched by $Na_2S_2O_3$ solution (50 μL) before analysis. For the recycle tests, the catalysts were separated and washed with deionized water several times, and then dried at 70 °C. The adsorption experiments were carried out with different initial pH (pH = 3.5, 5.8, and 10.5). The initial pH was adjusted by H_2SO_4 or NaOH after the addition of PMS. All experiments were carried out in duplicate or triplicates, and the data obtained were averaged.

2.4. Detection of the pollutants and intermediates

SIZ concentration was analyzed by reversed-phase high-performance liquid chromatography (Agilent, USA) with the Eclipse XDB C18 (5 μm, 4.6 × 250 mm). The mobile phase consisted of formic acid (0.1%) and acetonitrile with a ratio of 60:40 (v/v) at a flow rate of 1.0 mL/min, and the column temperature was set at 30 °C (Table S1). The intermediates of SIZ were measured by ultra-performance liquid chromatography combined with quadrupole time-of-flight mass spectrometry (UPLCQ-TOF-MS/MS, Agilent 1290 Infinity II UPLC with Agilent G6545 Q-TOF). The formic acid (0.1%) and methanol were used as mobile phases A and B, respectively. The flow was 0.2 mL/min and the gradient elution condition was shown in Table S2. The ion-transfer capillary temperature was 500 °C during the ESI-MS analysis. Furthermore, the scan range of intermediates mass was from 50 to 800 *m/z* with positive mode electrospray ionization (ESI+). Agilent InfinityLab Poroshell 120 EC-C18 column (2.1 × 50 mm, 1.9 μm) was used to separate samples with the column temperature at 40 °C. All the samples were filtered with 0.22 μm PTFE syringe filter discs.

2.5. Analytical methods

The structure and morphology of samples were confirmed by X-ray diffraction (XRD, Shimadzu, XRD-7000), scanning electron microscopy (SEM, SU-8010, Hitachi), transmission electron microscopy (TEM, FEI Talos F200x, FEI Company, USA), and high-resolution transmission electron microscopy (HRTEM, JEM-2100 F). The high-angle annular dark-field scanning transmission electron microscopy (HAADF-STEM) images were performed on an FEI Titan Themis apparatus with an X-FEG electron gun and a DCOR aberration corrector operating at 300 kV. X-ray photoelectron spectroscopy (XPS, AXIS Ultra DLD, Kratos Co.) was used to analyze the elemental composition and chemical oxidation state. The nitrogen adsorption and desorption curves were tested by the ASAP 2420 micromeritics instrument and the Brunauer-Emmett-Teller surface

area was analyzed by the Brunauer-Emmett-Teller model. Electron paramagnetic resonance (EPR) spectra were obtained on Bruker EMX plus X-band CW EPR spectrometer (microwave frequency, 9.83 GHz; microwave power, 2.00 MW). Total organic carbon (TOC) analyses were realized by TOC analyzer (Shimadzu TOC-L CPH). The graphitization of the catalysts was analyzed by Raman spectroscopy (HORIBA). Co K-edge X-ray absorption fine structure spectroscopy (XAFS) analyses were performed with Si (111) crystal monochromators at the BL14W Beam line at the Shanghai Synchrotron Radiation Facility (Shanghai, China). Co K-edge extended X-ray absorption fine structure (EXAFS) spectra were recorded in transmission/fluorescence mode. Negligible changes in the line shape and peak position of Co K-edge X-ray absorption near-edge structure (XANES) spectra were observed between two scans taken for a specific sample. Inductively coupled plasma optical emission spectrometer (ICP-OES) was used to detect the content of metal ions. The concentration of remaining PMS in the solution was measured by

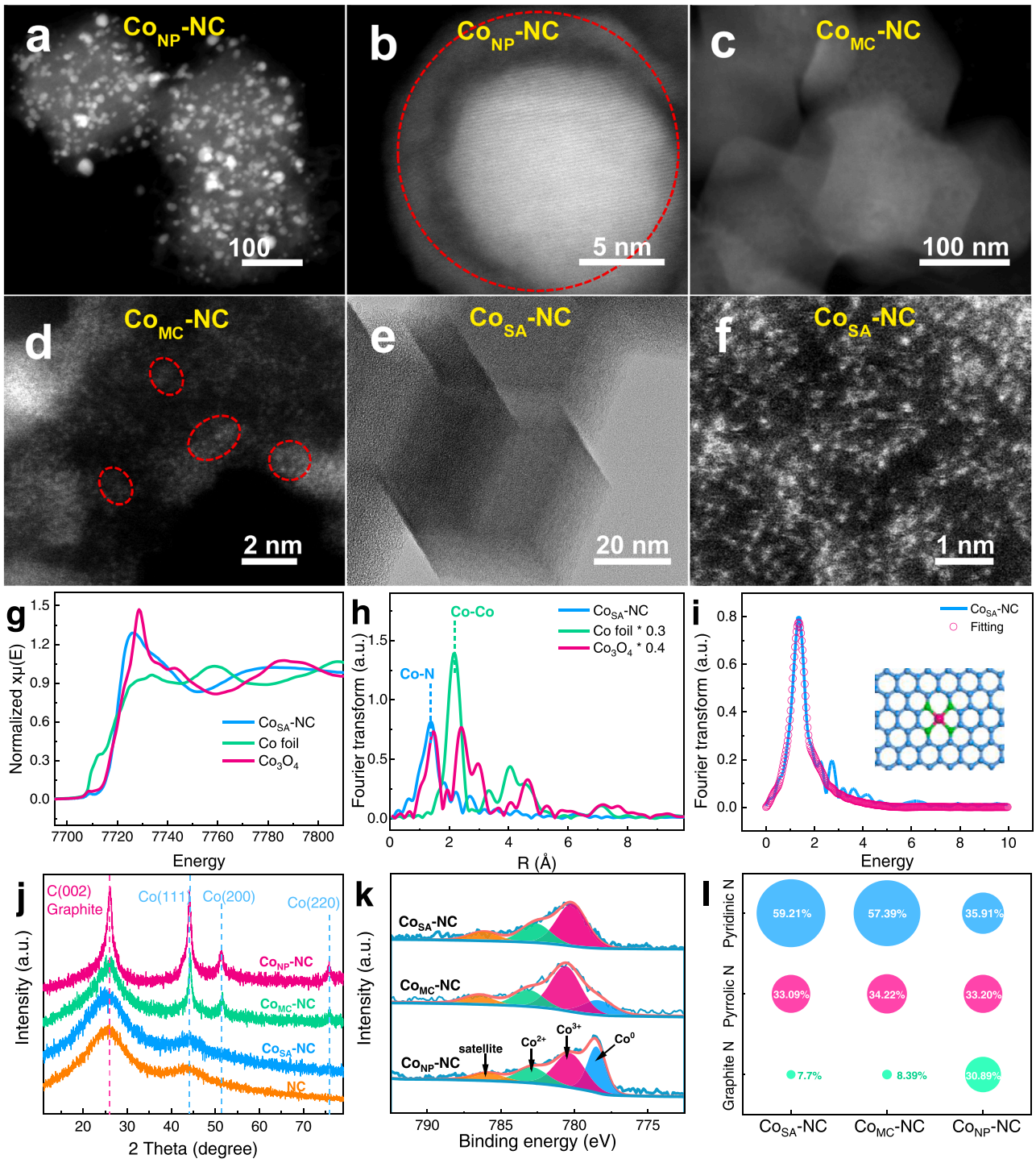

Fig. 1. Structural characterization: HAADF-STEM images and AC-HAADF-STEM images of (a-b) Co_{NP}-NC and (c-d) Co_{MC}-NC. (e) TEM images of Co_{SA}-NC. (f) AC-HAADF-STEM images of Co_{SA}-NC. (g) Co K-edge XANES spectra of Co foil, Co_3O_4, and Co_{SA}-NC. (h) k^3-weighted FT of the EXAFS spectra of Co foil, Co_3O_4, and Co_{SA}-NC. (i) Corresponding FT-EXAFS fitting curves of Co_{SA}-NC (Co-N_4 configurations in inset). (j) XRD patterns. (k) XPS Co 2p spectra in different catalysts, and (l) the relative ratio of N.

ABTS colorimetric method [10,26].

2.6. Electrochemical measurements

Electrochemical measurement was carried out on CHI 660E electrochemical workstation, using conventional three-electrode battery system, platinum as the opposite motor, saturated calomel electrode as reference electrode, and glassy carbon electrode as a working electrode. Place the three electrodes in a 50 mL beaker containing 0.5 M Na_2SO_4 solution of 25 mL. Among them, the glassy carbon electrode needs to be polished on the polishing cloth. The sample (4 mg), ethanol (960 μL), and Nafion reagent (40 μL) are mixed and dispersed ultrasonically for 30 min, and then uniformly covered on the conductive surface of the glassy carbon electrode. When the working electrode is air-dried, install the electrodes and start testing.

2.7. Computational methods

Computational methods: DFT calculations were conducted using Gaussian 16 package [27]. Geometry optimizations were performed using the B3LYP [28] functional with the 6–311 +G(d,p) basis set. Grimme's empirical dispersion correction [29] was employed in the calculations. Frequency analysis was subsequently conducted at the same level of theory to obtain the thermal corrections and confirm the stationary points as minima. Solvation effects were introduced using the integral equation formalism polarizable continuum model (IEF-PCM) [30] with water as the solvent. The condensed Fukui function (f^-, f^+, and f^0) [31] was calculated based on Hirshfeld charges [32] using the Multiwfn program [33].

3. Results and discussion

3.1. Characterization of the catalysts

The materials with different Zn/Co ratios have the same characteristic peaks as zeolitic imidazole framework (ZIF)− 8 in XRD spectrum, indicating that the configuration of the synthesized materials was the same as ZIF-8 (Fig. S2) [34]. After pyrolysis at 900 °C, the materials retained the original dodecahedral structures, with the identification of the SEM diagrams of NC, Co_{SA}-NC, Co_{MC}-NC, and Co_{NP}-NC (Fig. S3). Simultaneously, the particle size of the catalyst was shrunk with the decrease of Co content. Nanoparticles and clusters were formed in Co_{NP}-NC (Figs. 1a,b and S4a-d) and Co_{MC}-NC (Figs. 1c,d and S4e-h), respectively, according to the TEM images and aberration-corrected high-angle annular dark-field scanning transmission electron microscopy (AC-HAADF-STEM) images. Besides, the average diameters of nanoparticles and clusters (Fig. S5) were calculated to be 14.6 nm and 1.6 nm, respectively. As for Co_{SA}-NC, no nanoparticles or clusters are visible in the TEM diagrams (Fig. 1e). Meanwhile, AC-HAADF-STEM images revealed that brilliant spots of heavy atoms are spread in the Co_{SA}-NC, indicating that materials containing single-atom Co were synthesized in Co_{SA}-NC (Fig. 1f) [35].

The coordination environment and possible chemical state of single Co atoms in Co_{SA}-NC were revealed by XAFS measurements [36,37]. As depicted in the XANES spectra (Fig. 1g), the near-edge absorption energy of Co_{SA}-NC is located between the Co foil and Co_3O_4, suggesting that the oxidation state of Co in Co_{SA}-NC is between Co^0 and Co^{3+}. The k^3-weighted Fourier transform spectra of EXAFS (Fig. 1h) illustrated a prominent peak of Co_{SA}-NC at about 1.41 Å compared to the peak of Co-Co (2.2 Å) coordination in Co foil, which could be pointed the Co-N bond coordination [8]. To reinforce these results, wavelet-transform (WT) contour plots (Fig. S6) showed one intensity maximum at 3.5 $Å^{-1}$, assigning to the Co-N coordination. Furthermore, EXAFS fitting parameters at the Co K-edge were used to analyze the coordination of single Co atoms in Co_{SA}-NC (Fig. 1i, Fig. S7, and Table S3). The results revealed that the bond length was 1.89 ± 0.023 Å and the coordination number was 4.1 ± 0.2.

Besides, the crystalline phases and chemical structures of NC, Co_{SA}-NC, Co_{MC}-NC, and Co_{NP}-NC were determined by XRD (Fig. 1j). The peaks at 44.3°, 51.6°, and 75.9° indicate that metal Co grows along (111), (200), (220) crystal planes (JCPDS card 15–0806), while the characteristic peak at 26° belongs to graphitized carbon (JCPDS card 75–1621) [38,39]. With the decrease of Co content, the characteristic peak of Co gradually weakened, and no characteristic peak of Co was detected in Co_{SA}-NC (the characteristic peak was similar to NC), which was attributed to the formation of Co single atom. Besides, the broad diffraction peaks of Co_{SA}-NC and NC at around 44° were attributed to C (111) [40,41]. To further understand the structure of Co-NC catalysts, the elemental composition and valence states were compared in XPS spectra (the survey spectrum is shown in Fig. S8). Fig. 1k demonstrated that the Co $2p_{3/2}$ spectrum can be deconvoluted into Co^0 (778.7 eV), Co^{3+} (780.2 eV), Co^{2+} (782.0 eV), and satellite peak (786.5 eV) [7]. The peaks of Co^{3+} and Co^{2+} were main in Co_{SA}-NC, and the peak of Co^0 is absent, which indicated Co species are present as oxidation state rather than metallic state [42]. Fig. S9 was the high-resolution spectrum of N 1 s, which could be divided into pyridinic (398.8 eV), pyrrolic (400.1 eV), and graphene N (401.3 eV) [43], respectively. Interestingly, Fig. 1l and Table S4 show the pyridinic N decreases and the pyrrolic N increases by increasing Co content, indicating that isolated Co atoms are mostly immobilized with pyridinic N in Co_{SA}-NC. Meanwhile, the Co atom mainly exists in the form of Co^{3+}. However, graphene N and Co^0 are abundant in Co_{NP}-NC. In addition, the Raman spectra were employed to further investigate the graphitized state of catalysts. All the catalysts show two characteristic peaks at 1357 cm^{-1} and 1587 cm^{-1}, which were assigned to the D-band and G-band, respectively. Fig. S10 displays the value of I_G/I_D followed by 0.79, 0.89, 0.90, and 1.07 for NC, Co_{SA}-NC, Co_{MC}-NC, and Co_{NP}-NC, indicating that a smaller scale of Co active sites results in a low graphitization degree and high defects/disorders [44,45]. Besides, the nitrogen adsorption and desorption curves reveal that the specific surface area of Co_{SA}-NC is 827 m^2/g and the pore size is 3.64 nm (Fig. S11 and Table S5). The specific surface area of Co_{MC}-NC and Co_{NP}-NC is lower due to the destruction of the C matrix by the introduction of more Co particles (646 m^2/g and 434 m^2/g). However, Table S5 showed the pore size of Co_{MC}-NC (4.11 nm) and Co_{NP}-NC (6.71 nm) is larger than Co_{SA}-NC (3.64 nm). The aforesaid results validated the effective synthesis of the different active center sizes of Co_{SA}-NC, Co_{MC}-NC, and Co_{NP}-NC.

3.2. Performance of the catalysts

The catalytic performances of Co_{SA}-NC, Co_{MC}-NC, and Co_{NP}-NC were evaluated for SIZ removal in the presence of PMS. Specific analysis of the effect of catalyst and PMS dosage on the removal efficiencies of SIZ is elaborated in Supporting Information (Text S1 and Fig. S12), and the optimal dosage of catalyst and PMS was 150 mg/L and 0.3 mM, respectively. As shown in Fig. S12a, there is only 15% SIZ was removed in the sole PMS system and 40% in NC/PMS after 30 min reaction, which means that Co sites play a significant role in these catalysts. Besides, Fig. S12d revealed a wide pH adaptation range of Co_{SA}-NC/PMS for the SIZ (pKa = 5.00) degradation. And the pH value of Co_{SA}-NC system changed from 5.8 to 3.5 with the PMS added (Fig. S13). It needs to be emphasized that the reaction time of subsequent experiments was shortened to 20 min due to more than 70% of SIZ can be degraded in 5 min for three catalytic systems. In addition, as shown in Fig. S14, the adsorption capacity of catalysts for the SIZ under different initial pH (pH = 3.5, 5.8, or 10.5) was diminished with the increase of pH value, which because the OH^- in solution would react with active sites that inhibited the adsorption efficiency of catalysts [46–48]. Furthermore, the adsorption of SIZ decreased with the transformation of Co sites from Co_{NP}-NC to Co_{SA}-NC under the acidic condition (pH = 3.5). It may be caused by the pore size becoming smaller with the change of Co sites from Co_{NP}-NC to Co_{SA}-NC, which limits its adsorption capacity as

illustrated in Fig. S11 and Table S5. In the presence of PMS, 99% removal of SIZ was achieved in Co_{SA}-NC, Co_{MC}-NC, and Co_{NP}-NC systems after 20 min of treatment (Fig. 2a). To further investigate the activity of catalysts, the first-order kinetic model was employed to fit SIZ degradation profiles. The pseudo first-order rate constant (k_{obs}) of SIZ in Co_{SA}-NC/PMS, Co_{MC}-NC/PMS, and Co_{NP}-NC/PMS were 0.248 min^{-1}, 0.247 min^{-1}, and 0.367 min^{-1}, respectively (Fig. S15). Moreover, as illustrated in Fig. S16, desorption experiments indicated that the concentrations of desorbed SIZ from adsorption equilibrium catalysts were 1.95 mg/L (Co_{SA}-NC), 2.12 mg/L (Co_{MC}-NC), and 2.23 mg/L (Co_{NP}-NC) without PMS addition. But the desorbed SIZ was negligible with PMS added in three catalytic systems (the details of desorption experiments are shown in Text S2). The synergistic action of adsorption and oxidation aided in the quick removal of SIZ from wastewater [23]. Likewise, compared to the sole PMS system, the PMS decomposition rates of Co_{SA}-NC/PMS, Co_{MC}-NC/PMS, and Co_{NP}-NC/PMS systems were all over 90% (Fig. S17), exhibiting relatively vigorous efficiency for PMS activation.

Moreover, as depicted in Fig. 2b and Fig. S18, Co_{SA}-NC, Co_{MC}-NC, and Co_{NP}-NC exhibited high stability for PMS activation to degrade SIZ. The degradation rate of SIZ was kept at 100% after 5 cycle reaction (the recovery method of catalysts is shown in Text S3). To further estimate the influence of leaching Co ions (the process of experiment was described in Fig. S19), the reacted solution was filtered to be tested for SIZ degradation under a similar condition, whose k_{obs} was 0.009 min^{-1} (the homogeneous of Co_{SA}-NC), 0.058 min^{-1} (the homogeneous of Co_{MC}-NC), and 0.101 min^{-1} (the homogeneous of Co_{NP}-NC) (Fig. S19). Especially the homogeneous phase of Co_{SA}-NC could be ignored. Also, the concentration of Co ions dissolved into the solution had a great decrease in the fifth round (Fig. S20). Besides, the presence of coexisting anionic ions (i.e., Cl^-, NO_3^-, HCO_3^-, and $H_2PO_4^-$) or actual water (i.e., lake water, tap water, and river water) had almost no impact on the removal of pollutant in the three systems (Fig. S21-22). The results indicated that three catalysts have good efficiency and stability for PMS activation to remove SIZ.

3.3. Determination of ROS and the mechanism for activating PMS

The quenching tests for Co_{SA}-NC, Co_{MC}-NC, and Co_{NP}-NC catalysts were used to analyze active species. Interestingly, the addition of TBA (300 mM) and MeOH (300 mM) as scavengers to inhibit free radicals ($^{\bullet}OH$ and $SO_4^{\bullet-}$) in the Co_{SA}-NC/PMS, Co_{MC}-NC/PMS, or Co_{NP}-NC/PMS

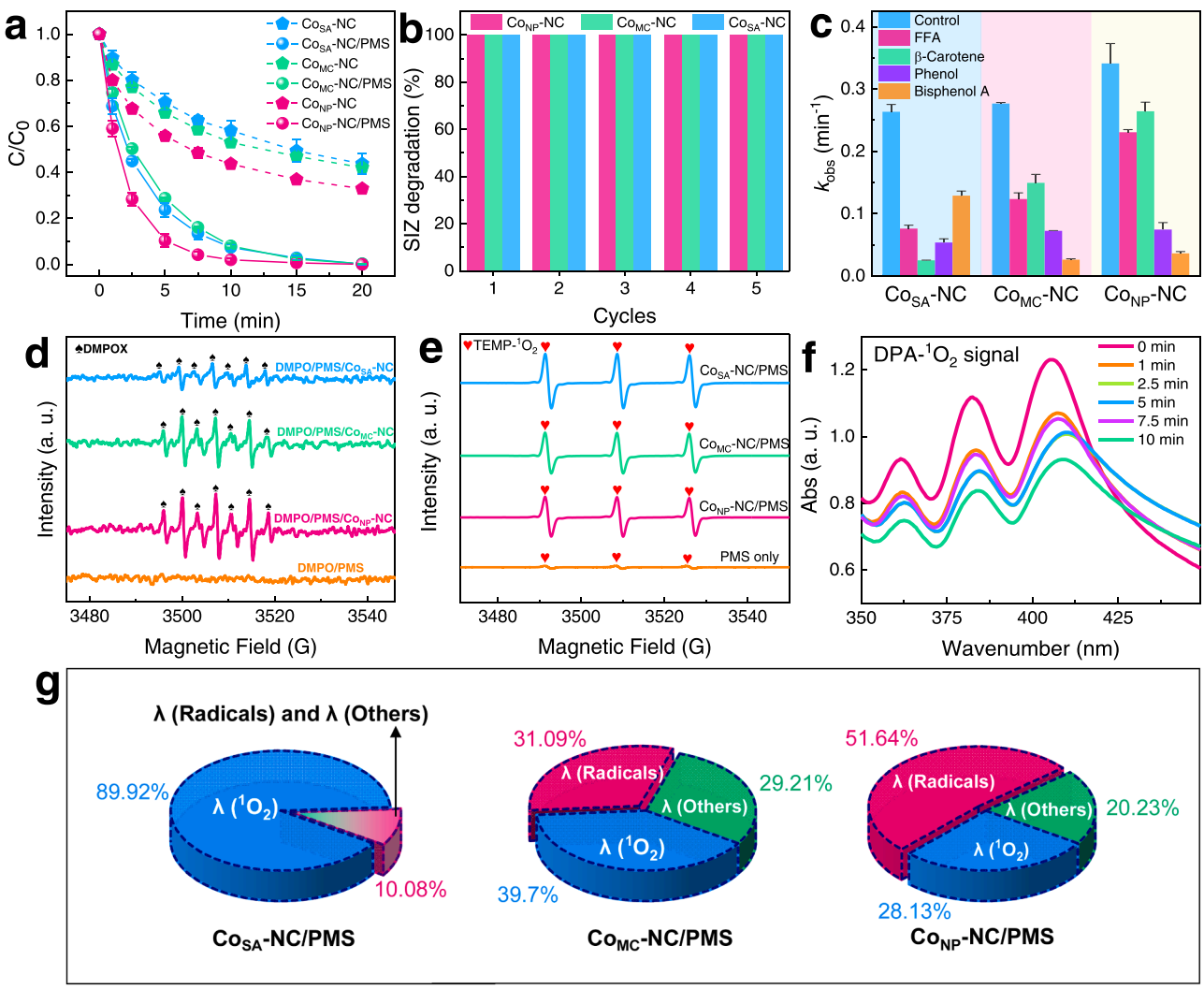

Fig. 2. The performances of (a) Co_{SA}-NC/Co_{MC}-NC/Co_{NP}-NC activated PMS to remove SIZ. (b) The changes of SIZ degradation efficiency in several cycling times by different systems (every reaction was 20 min). (c) The k_{obs} of different quenchers towards Co_{SA}-NC/Co_{MC}-NC/Co_{NP}-NC to remove SIZ. EPR spectra in Co_{SA}-NC/PMS, Co_{MC}-NC/PMS, and Co_{NP}-NC/PMS systems with DMPO (d) and TEMP (e) as the trapping agent. (f) UV spectra of DPA degradation in Co_{SA}-NC/PMS system. (g) The proportion of $^1O_2$ and radicals ($SO_4^{\bullet-}$ and $^{\bullet}OH$) in different catalytic systems. Experimental conditions: $[catalyst]_0$ = 150 mg/L, $[PMS]_0$ = 0.3 mM, $[SIZ]_0$ = 5 mg/L, $[TBA]_0$ = 300 mM, $[FFA]_0$ = 10 mM, $[\beta\text{-Carotene}]_0$ = 0.1 mM, $[phenol]_0$ = 50 mg/L, $[BPA]_0$ = 50 mg/L, $[BA]_0$ = 10 mg/L, $[NB]_0$ = 10 mg/L, and $[DPA]_0$ = 1 g/L.

systems could hardly influence the degradation of SIZ (Fig. S23). According to searching the second-order rate constants for reactions of several organics with ROS, suggesting that the reaction rate constants of SIZ with $^{\bullet}OH$ and $SO_4^{\bullet-}$ ($k^{\bullet}OH_{,\ SIZ} = 6.6 \times 10^9\ M^{-1}\ s^{-1}$, $kSO_4^{\bullet-}{}_{SIZ} = 1.6 \times 10^9\ M^{-1}\ s^{-1}$) are higher than the MeOH ($k^{\bullet}OH_{,\ MeOH} = 9.7 \times 10^8\ M^{-1}\ s^{-1}$, $kSO_4^{\bullet-}{}_{MeOH} = 2.5 \times 10^7\ M^{-1}\ s^{-1}$) and TBA ($k^{\bullet}OH_{,\ TBA} = 6.6 \times 10^8\ M^{-1}\ s^{-1}$, $kSO_4^{\bullet-}{}_{TBA} = 7.7 \times 10^7\ M^{-1}\ s^{-1}$) [49–52]. Hence, the MeOH and TBA could not efficiently inhibit the reactions between SIZ and $^{\bullet}OH$ and $SO_4^{\bullet-}$. To further investigate the contribution of radicals ($^{\bullet}OH$ and $SO_4^{\bullet-}$), phenol and BPA were selected as scavengers competing with SIZ for ROS due to the higher second-order rate constants with ROS (Table S6). Fig. 2c depicted that the k_{obs} of SIZ sharply decreased with the addition of excessive phenol in three catalytic systems. Also, the addition of BPA had an obviously inhibitory effect on Co_{MC}-NC/PMS and Co_{NP}-NC/PMS. But the inhibition of BPA on Co_{SA}-NC/PMS was less than in the former two systems (Fig. S24). It was explained that the $k^1O_{2,\ BPA} = 7.99 \times 10^5\ M^{-1}\ s^{-1} < k^1O_{2,\ Phenol} = 2.6 \times 10^6\ M^{-1}\ s^{-1} < k^1O_{2,\ SIZ} = 9.7 \times 10^6\ M^{-1}\ s^{-1}$. The results illustrated that phenol and BPA could efficiently inhibit the reactions between SIZ and $^{\bullet}OH$ and $SO_4^{\bullet-}$. However, the similar second-order rate constants for reactions of SIZ, phenol, and BPA with $^1O_2$ make it necessary to further give priority to the contributions of $^1O_2$ in the systems.

Generally, FFA as a scavenger could be used for $^1O_2$ detection [39, 53]. Fig. 2c delineated the k_{obs} of SIZ degradation decreased from 0.248 min^{-1} (Co_{SA}-NC), 0.247 min^{-1} (Co_{MC}-NC), and 0.367 min^{-1} (Co_{NP}-NC) to 0.076 min^{-1}, 0.123 min^{-1}, and 0.230 min^{-1} with FFA adding, respectively. But it was reported that FFA can also consume $^{\bullet}OH$ with a high reaction rate constant ($k^{\bullet}OH_{,\ FFA} = 1.5 \times 10^{10}\ M^{-1}\ s^{-1}$, as shown in Table S6) [49]. Further, the β-carotene as a scavenger for $^1O_2$ with a high reaction rate constant ($k^1O_{2,\ \beta\text{-carotene}} = 2.0–3.0 \times 10^{10}\ M^{-1}\ s^{-1}$) was carried out with a pure MeOH solution [50]. Fig. S25a showed that the pure MeOH solution had weak effects on the SIZ removal rate. Hence, the contribution of $^1O_2$ was analyzed in pure MeOH solution with β-carotene adding, and Fig. 2c exhibited the degradation rate of Co_{SA}-NC/PMS system for SIZ was obviously inhibited, which the k_{obs} decreased from 0.248 min^{-1} to 0.025 min^{-1}. Besides, the Co_{MC}-NC/PMS and Co_{NP}-NC/PMS were also inhibited with the β-carotene added in pure MeOH (Fig. 2c and S25b-d). The aforementioned quenching experiments demonstrated that the $^1O_2$ was the main ROS in Co_{SA}-NC/PMS, and the radicals had more contribution in Co_{MC}-NC/PMS and Co_{NP}-NC/PMS systems.

EPR experiments were performed to further distinguish the active species of the three systems. EPR spectra using DMPO for trapping $^{\bullet}OH$ and $SO_4^{\bullet-}$ and TEMP for trapping $^1O_2$ in Co_{SA}-NC, Co_{MC}-NC, and Co_{NP}-NC systems were shown in Fig. 2d,e [54–56]. Interestingly, the EPR signals of DMPO-$SO_4^{\bullet-}$ and DMPO-$^{\bullet}OH$ could not be observed (Fig. 2d). Contrarily, the seven peaks signal ($\alpha^N = 7.3 \pm 0.1$ G and $\alpha^H = 3.9 \pm 0.1$ G) was recorded, which attributed to the DMPO-X [10,57]. And the intensity of the seven peaks signal was increasing with the size growth of Co sites. The DMPO-X suggests that highly reactive oxygen-containing species were generated in the process of PMS activation [58]. Moreover, the strong typical 3-fold characteristic peaks ($\alpha^N = 17.24$ G) [39] of the TEMP-$^1O_2$ adduct were observed in Co_{SA}-NC/PMS, Co_{MC}-NC/PMS, and Co_{NP}-NC/PMS systems compared to PMS only (Fig. 2e).

To further identified the radical species, BA and NB were used as the probe compound for radical determination [10]. Fig. S26 depicts the adsorption of BA presented in three catalyst systems, and all of them could adsorb saturation in 30 min. In comparison to the Co_{SA}-NC/PMS and Co_{MC}-NC/PMS systems, the Co_{NP}-NC/PMS system removes BA more effectively, and the degradation was reduced by the addition of MeOH. The results further prove that the radicals ($^{\bullet}OH$ and $SO_4^{\bullet-}$) are produced in large quantities in Co_{NP}-NC/PMS system. In contrast, the degradation of BA in the Co_{SA}-NC/PMS could be ignored. Thus, it can be concluded that the radicals ($^{\bullet}OH$ and $SO_4^{\bullet-}$) are not the main active species in the Co_{SA}-NC/PMS system. As for the Co_{MC}-NC/PMS system, the removal efficiency of BA is lower than the Co_{NP}-NC/PMS system. However, the degradation of BA was inhibited with the addition of MeOH. Similarly, the NB removal trend shows the same situation as BA degradation. The NB degradation rates are 12.86%, 37.03%, and 41.63% corresponding to Co_{SA}-NC, Co_{MC}-NC, and Co_{NP}-NC, respectively (Fig. S27). The results further suggested that the contribution of the $^{\bullet}OH$ and $SO_4^{\bullet-}$ was decreasing with the diminution of Co size from Co_{NP}-NC to Co_{SA}-NC. For the same purpose, the generation of $^1O_2$ was further proved by the oxidation of 9,10-diphenylanthraquinone dyes (DPA) (Text S4) [59]. Fig. 2 f demonstrated that the intensity of the absorption peak near 378 nm weakened gradually in the first 5 min, which indicated the continuous generation of $^1O_2$. However, the peak intensity of 7.5 min was stronger than the 5 min, suggesting that the accumulation of $^1O_2$ was reduced due to the consumption of PMS. Besides, it was observed in Fig. S28 that the intensity of the absorption peak near 378 nm in the Co_{MC}-NC system and Co_{NP}-NC system decreased more slowly than Co_{SA}-NC system. The results ulteriorly suggested that the contribution of $^1O_2$ gradually dominated with the scale of Co site from nanoparticles to single atoms in PMS activation systems.

In addition, it reported that a direct electron transfer mechanism from contaminants (electron donor) to PMS (electron acceptor) was performed in PMS activation systems [8,60,61]. In this work, the mentioned electron transfer between SIZ, catalysts, and PMS was tested by Tafel, open-circuit potential, and the salt bridge experiments. Tafel diagrams revealed that the corrosion potentials of Co_{SA}-NC, Co_{MC}-NC, and Co_{NP}-NC were 0.143, 0.239, and 0.419 V, respectively, implying that the electron transfer rate was Co_{NP}-NC > Co_{MC}-NC > Co_{SA}-NC (Fig. 3a). Meanwhile, the electrochemical workstation calculated the corrosion current values (Table S7), which corresponded to the results of the corrosion potential. Moreover, the intrinsic electron transfer kinetics was examined by open-circuit potential test (Fig. 3b). The open-circuit potentials of glassy carbon electrode (GCE) coated with catalysts were drastically enhanced with the dosing of PMS, while the SIZ addition reduced the potential. The formation of reactive PMS complex on the surface of the catalyst could elevate the potential of catalysts, while the reaction between SIZ and the surface reactive PMS complex resulted in a reduction of potential [8]. Additionally, premixed experiments were carried out to test the reaction between PMS and catalysts without SIZ. Fig. S29 illustrated that the SIZ removal efficiency decreased a lot after premixed experiments in three systems. However, the contribution of the electron transfer pathway to remove SIZ was unclear in three systems. The salt bridge experiments (Fig. 3c) further explored the contribution of the direct electron transfer process, which illustrated that the current fluctuation was observed in three systems, but the SIZ degradation rate kept bellowing at 10%. The results indicated that the contribution of the direct electron transfer process was not the main role. Furthermore, it reported that high-valent cobalt-oxo species is the main active species in the Co^{2+}/PMS process under acidic conditions [62]. Hence, the PMSO degradation and $PMSO_2$ production were detected in three systems (Fig. S30). The η_{PMSO2} (η_{PMSO2} = the production of $PMSO_2$/the consumption of PMSO) followed 20.64%, 39.71%, and 66.24% from Co_{SA}-NC to Co_{NP}-NC, but the degradation rates of PMSO were poor, which indicates the high-valent cobalt-oxo species can be ignored in those systems. Besides, as shown in Fig. S31, the inhibition of the three systems by BQ, DMSO, and EDTA was not significant and also excluded the generation of superoxide anion radical ($^{\bullet}O_2^-$) as well as surface active species [63,64].

In conclusion, as shown in Fig. 2 g, the contribution of $^1O_2$ for SIZ degradation increased from 28.13% to 89.92%, and radicals ($^{\bullet}OH$ and $SO_4^{\bullet-}$) contribution decreased from 51.64% to less than 10.08%, with the Co sizes from nanoparticles to single atoms (the detail in Text S5 and Eq. (S1-S6)). The generation of different ROS exited strongly active center size-dependent of catalysts for PMS activation. The Co single atom sites enhanced the nonradical process, which was a $^1O_2$ dominant process. While the Co sites transformed into nanoparticles, the radical process ($^{\bullet}OH$ and $SO_4^{\bullet-}$) played a dominant role in the reaction. As for

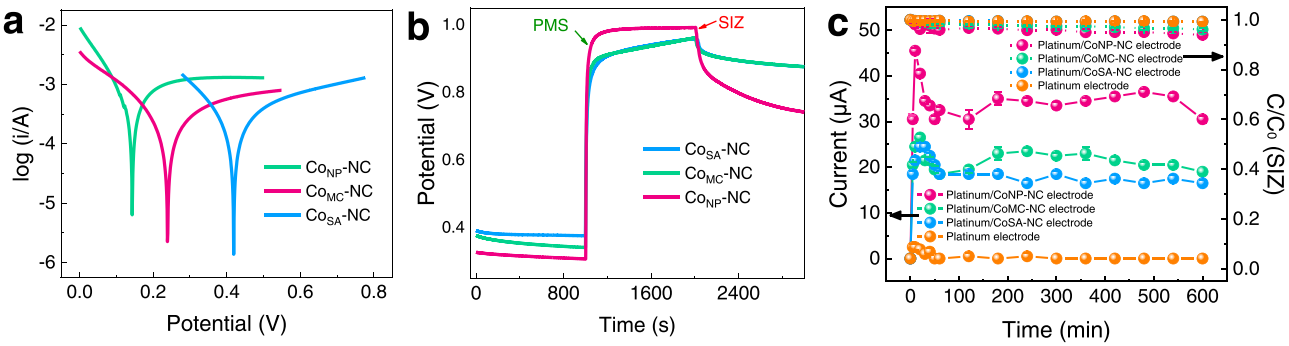

Fig. 3. (a) Tafel polarization curves, (b) open-circuit potential, (c) the results of salt bridge experiments.

Co_{MC}-NC, both radical and nonradical processes showed weaker contributions compared to the Co_{NP}-NC and Co_{SA}-NC.

3.4. Switching the primary degradation route and biotoxicity of SIZ

Interestingly, the different peaks of byproducts were detected in the three catalytic systems as shown in the liquid chromatogram (Fig. S32). The phenomenon may suggest that the degradation routes of SIZ were switched with the active center size-dependent catalysts for PMS activation. Therefore, the degradation byproducts of SIZ were detected by UPLC-QTOF-MS/MS in Co_{SA}-NC/PMS, Co_{MC}-NC/PMS, and Co_{NP}-NC/PMS systems (Table S8 and Fig. S33-S57). Combined with the results of UPLC-QTOF-MS/MS, the active sites of organic molecules were illustrated by the Fukui index (Fig. 4a,b). Generally, the values of electrophilic (f^-), radical (f^0), and nucleophilic (f^+) might potentially reflect the relative activity of each atom in the SIZ molecule. The reactive sites with high f^- value are easiest to electrophilic species (such as $^1O_2$) [65, 66]. The f^0 value could indicate the regioselectivity of radical species ($^{\bullet}OH$ and $SO_4^{\bullet-}$) [23]. As shown in Fig. S58, the darker the blue part of SIZ was, the more vulnerable to attack it was. The electrophilic reaction shown in Fukui function color-filled isosurface maps of f^- was mainly concentrated in N7, C15, and C16. The free radical attack region shown in Fukui function color-filled isosurface maps of f^0 moved towards the benzene ring relative to Fukui function color-filled isosurface maps of f^-, mainly in the two adjacent positions C of N7. In addition, a blue area also appeared near S1, which means that it was also vulnerable to free radical attack (Fig. S58b). The highest occupied molecular orbital (HOMO) implied that electrons are easy to escape from the regions of SIZ and be attacked by $^1O_2$ (Fig. S59) [23,65].

Furthermore, four possible main degradation pathways were proposed according to the results of DFT calculation and intermediates (Fig. 4c). For pathway I, P1-P4 were detected in three systems (Co_{SA}-NC/PMS, Co_{MC}-NC/PMS, and Co_{NP}-NC/PMS), which benefit from the unselective $^{\bullet}OH$, $SO_4^{\bullet-}$ process. The S−N bond was attacked and then the −OH or −H was added. Also, pathway I was reported by plentiful advanced oxidation processes (AOPs) for sulfonamides degradation [67, 68]. In pathway II, P5 and P6 were mainly detected in both Co_{MC}-NC/PMS, and Co_{NP}-NC/PMS systems, which is mainly a hydroxylation process. Production of P5 was attributed to the attacking of $^{\bullet}OH/SO_4^{\bullet-}$ and hydroxylation. Furthermore, the S−N bond of P5 was oxidized to broken, producing P6 and P2. The result is consistent with the previous high f^0 values of S1 and C15/C16. In pathway III, N11 of SIZ with high f^- value was attended to be attacked by $^1O_2$. Notably, the P7, P8, and P9 were mainly detected in the Co_{SA}-NC/PMS system, that the amine group of SIZ experienced hydroxylation, nitrosation, and nitrification in sequence. The phenomenon may be ascribed to the $^1O_2$ being more likely to attack an electron-rich site like N11 of SIZ, but the non-selective oxidation of radicals can further oxidize the SIZ through pathway I/II. Pathway III was also found from the $^1O_2$ oxidation of sulfonamides by photo-transformation and PMS activation [9,68]. As for pathway IV, the production of P10 was caused by the breaking of the N − C bond, which is a classical oxidative product of SIZ. However, the

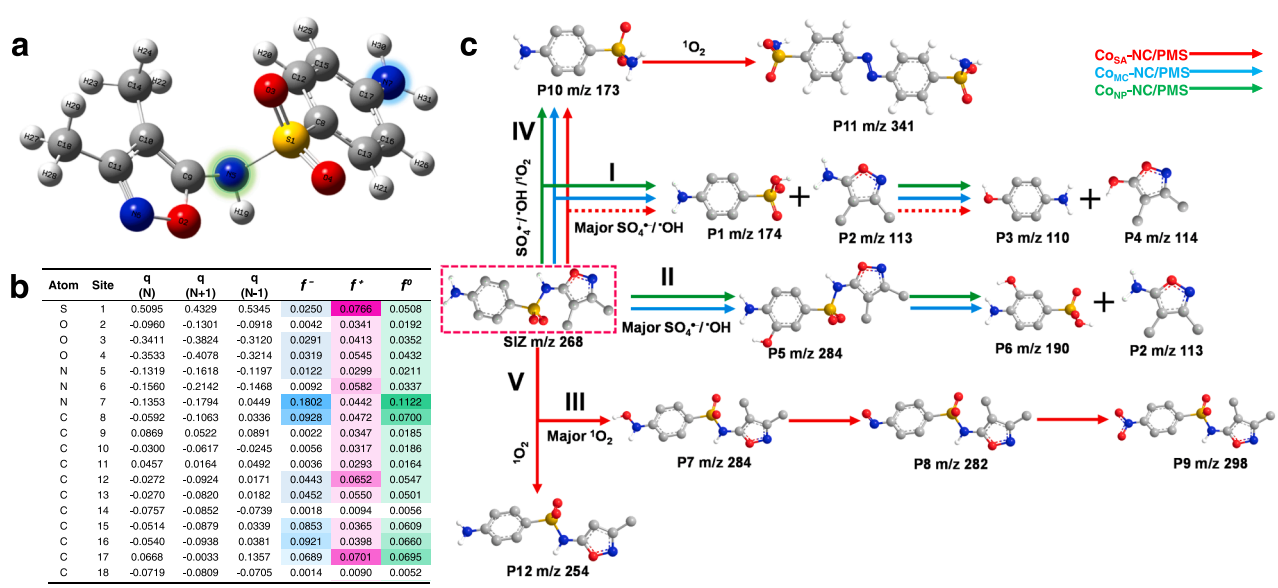

Atom	Site	q (N)	q (N+1)	q (N-1)	f^-	f^*	f^0
S	1	0.5095	0.4329	0.5345	0.0250	0.0766	0.0508
O	2	-0.0960	-0.1301	-0.0918	0.0042	0.0341	0.0192
O	3	-0.3411	-0.3824	-0.3120	0.0291	0.0413	0.0352
O	4	-0.3533	-0.4078	-0.3214	0.0319	0.0545	0.0432
N	5	-0.1319	-0.1618	-0.1197	0.0122	0.0299	0.0211
N	6	-0.1560	-0.2142	-0.1468	0.0092	0.0582	0.0337
N	7	-0.1353	-0.1794	0.0449	0.1802	0.0442	0.1122
C	8	-0.0592	-0.1063	0.0336	0.0928	0.0472	0.0700
C	9	0.0869	0.0522	0.0891	0.0022	0.0347	0.0185
C	10	-0.0300	-0.0617	-0.0245	0.0056	0.0317	0.0186
C	11	0.0457	0.0164	0.0492	0.0036	0.0293	0.0164
C	12	-0.0272	-0.0924	0.0171	0.0443	0.0652	0.0547
C	13	-0.0270	-0.0820	0.0182	0.0452	0.0550	0.0501
C	14	-0.0757	-0.0852	-0.0739	0.0018	0.0094	0.0056
C	15	-0.0514	-0.0879	0.0339	0.0853	0.0365	0.0609
C	16	-0.0540	-0.0938	0.0381	0.0921	0.0398	0.0660
C	17	0.0668	-0.0033	0.1357	0.0689	0.0701	0.0695
C	18	-0.0719	-0.0809	-0.0705	0.0014	0.0090	0.0052

Fig. 4. (a) Chemical structure and atom order of SIZ. (b) The Fukui index of SIZ. (c) Possible transformation pathways of SIZ in Co_{SA}-NC/PMS, Co_{MC}-NC/PMS, and Co_{NP}-NC/PMS systems.

P11 was only detected in Co_{SA}-NC/PMS system. It was reported that product P11 was formed by the attacking of $^1O_2$, which is the reaction of diazo coupling via product P10 [9,68]. Moreover, P9 was also detected because a methyl group of SIZ was removed. The results indicated that the degradation routes of SIZ could be regulated by the evolution of ROS from the systems of active center site-dependent catalysts. Besides, multiple pollutants can be efficiently removed in three systems (Fig. S60a). And BPA was selected to further evaluate the universality of the switching mechanisms of pollutant degradation routes in active center size-dependent catalysts. As shown in Fig. S60b, the different intermediates were performed in three catalytic systems. Compared to the blank samples, six new peaks were generated. The $P_{(BPA)}3$, $P_{(BPA)}4$, and $P_{(BPA)}5$ were mainly in Co_{SA}-NC system, but the $P_{(BPA)}1$ was in Co_{NP}-NC and Co_{MC}-NC. This result implied that modulation of degradation routes can be achieved by active center size-dependent catalysts in Fenton-like reaction.

As the application potential manifestation of three different systems, the toxicity assessment of SIZ and intermediate products was executed to analyze the mutagenicity, acute toxicity, bioaccumulation factor, and developmental toxicity via the Toxicity Estimation Software Tool (T.E.S.T., US, EPA) [69]. As an exhibition in Fig. 5a, all the intermediates other than P4 have negative mutagenicity. For acute toxicity of oral rat LD_{50}, all the products have lower acute toxicity of oral rat LD_{50} than SIZ (8227.12 mg/kg), implying the acute toxicity of intermediates increased, especially the oral rat LD_{50} of P3 is 262.39 mg/kg (Fig. 5b). Besides, the bioaccumulation factor (Fig. 5c) shows that all intermediates have lower toxicity than SIZ. Additionally, for developmental toxicity, some intermediates have lower toxicity than SIZ, but several more toxic intermediates are produced (Fig. 5d). The results indicate that the toxicity of SIZ can be weakened after the treatment process, but some intermediates are still relatively toxic.

Also, to assess the potential risk of intermediates, the photobacterium of *Vibrio fischeri* was carried out to examine the biological toxicity of three catalytic systems (the details in Text S6) [70,71]. The inhibition rate ($IR_{SIZ\ and\ its\ intermediates}$) of SIZ and intermediates for *Vibrio fischeri* after 20 min treatment followed: Co_{SA}-NC/PMS/SIZ < Co_{MC}-NC/PMS/SIZ < Co_{NP}-NC/PMS/SIZ (Figs. 5e, S61 and Table S9). Interestingly, Fig. 5f demonstrated that the TOC removal rate followed 33.36%, 40.50%, and 55.98% corresponding to Co_{SA}-NC, Co_{MC}-NC, and Co_{NP}-NC. The results indicated that the strongly oxidizing properties of radicals ($^{\bullet}OH$ and $SO_4^{\bullet-}$) lead to a high mineralization degree of SIZ, but the non-selective oxidation may produce some more toxic byproducts. As for $^1O_2$, mineralization ability is weaker than $^{\bullet}OH$ and $SO_4^{\bullet-}$, but the characteristic of selective oxidation could avoid the generation of some more toxic intermediates at a certain [72]. Therefore, combined with practical application scenarios, it seems to be able to provide guiding values for PMS-AOPs. The radical pathway is more suitable for the situation requiring higher mineralization rates, while the $^1O_2$ pathway is more preferred for the selective oxidation process.

Finally, the switching mechanisms of ROS generation and pollutant degradation routes in active center size-dependent catalysts for PMS activation are summarized in Fig. 6. The Co site scale was regulated by controlling the Co loading to synthesize Co_{SA}-NC, Co_{MC}-NC, and Co_{NP}-NC. Three catalysts exhibited excellent SIZ degradation efficiencies and stabilities. The contribution of $^1O_2$ for SIZ degradation follows 89.92%, 39.7%, and 28.13% in Co_{SA}-NC, Co_{MC}-NC, and Co_{NP}-NC systems, respectively. Also, the $^{\bullet}OH$ and $SO_4^{\bullet-}$ proportion for SIZ removal was 51.64%, 31.09%, and less than 10.08% corresponding to Co_{NP}-NC,

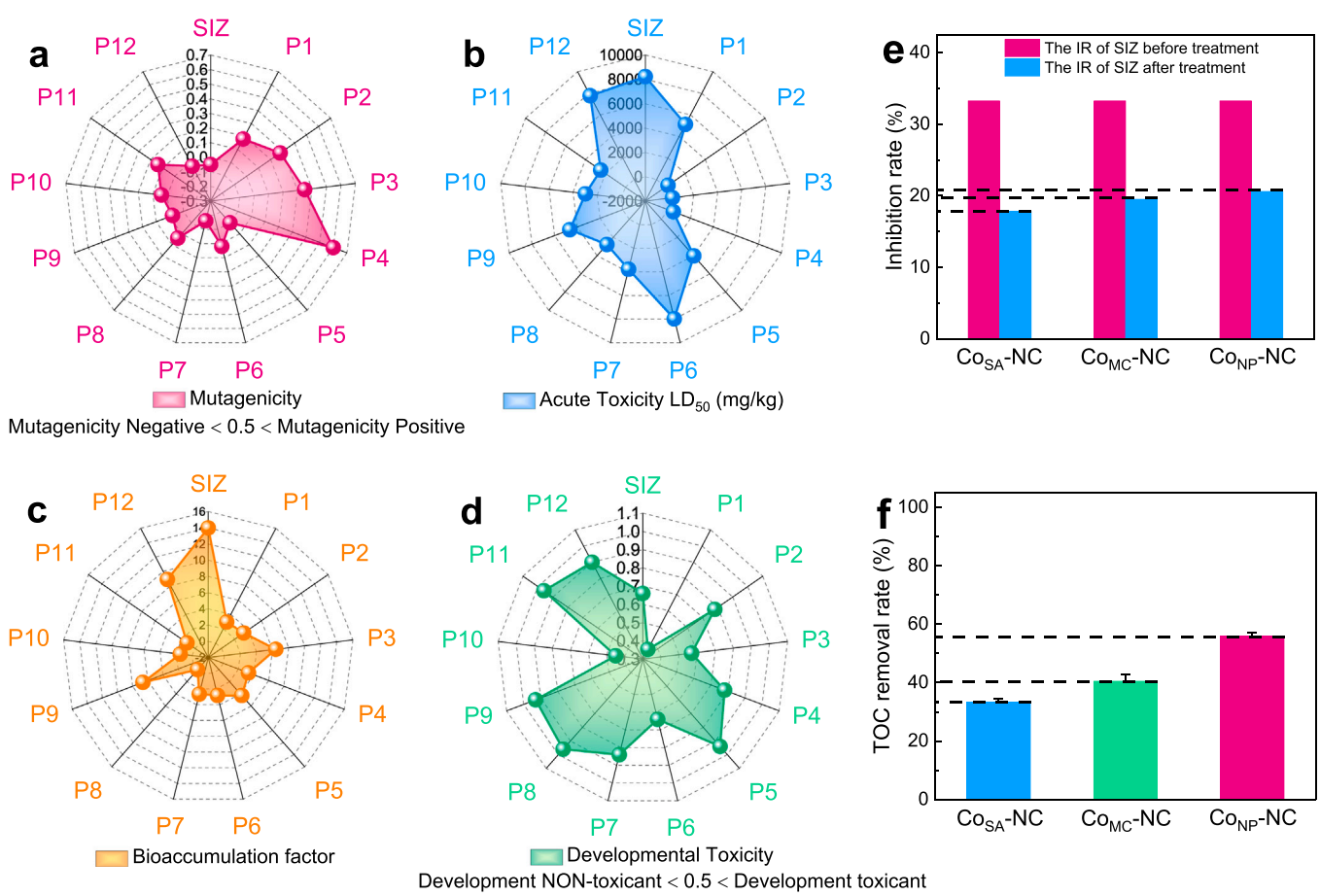

Fig. 5. (a) Mutagenicity, (b) acute toxicity, (c) bioaccumulation factor, and (d) developmental toxicity of SIZ and intermediates. The inhibition rate (IR) of SIZ before/after reaction on *Vibrio fischeri*. (f) The TOC removal rate of different systems.

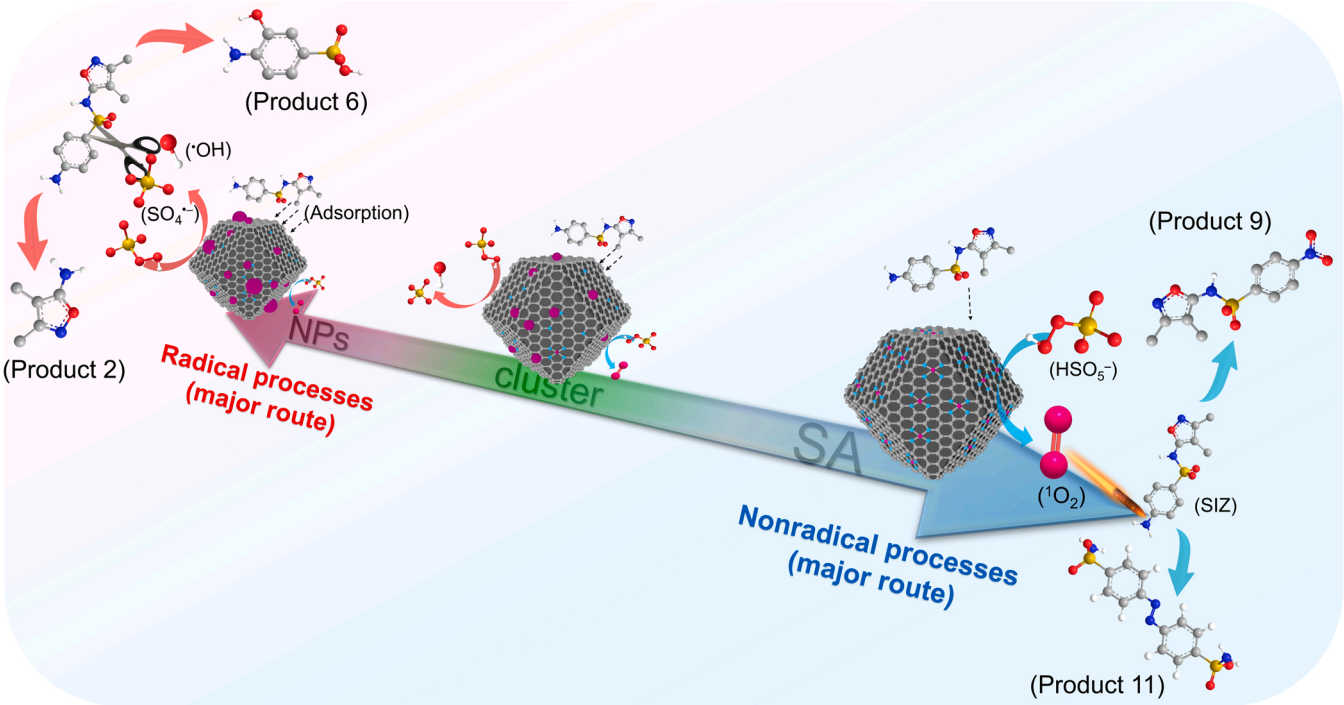

Fig. 6. Catalytic mechanisms of active center size-dependent catalysts for PMS activation.

Co_{MC}-NC, and Co_{SA}-NC, respectively. Hence, the evolution from $^{\bullet}OH$ and $SO_4^{\bullet-}$ to $^1O_2$ was achieved with the scale of Co site from nanoparticles (NPs) to single atom (SA). Significantly, $^1O_2$ is the main active species in the Co_{SA}-NC/PMS, which tends to react with the amino group of SIZ, contributing to selective oxidation. However, the radical process produces some intermediates with higher toxicity during the SIZ degradation due to non-selective oxidation.

4. Conclusion

In this work, the active center size-dependent catalysts (Co_{SA}-NC, Co_{MC}-NC, and Co_{NP}-NC) were successfully synthesized by rational designing. Three catalysts have excellent performance on PMS activation for SIZ removal, which also achieved the transformation of ROS. The radicals ($^{\bullet}OH$ and $SO_4^{\bullet-}$: 51.64%) exhibited a dominant role in Co_{NP}-NC/PMS, while $^1O_2$ (the proportion of 89.92%) played a significant role in SIZ degradation in Co_{SA}-NC/PMS. More importantly, the degradation routes of SIZ were switched by the evolution of ROS. The abundant $^1O_2$ that presents in the Co_{SA}-NC/PMS tends to attack the electron-rich site of SIZ, which occurs to addition, diazo coupling, and nitration. While radical ($^{\bullet}OH$ and $SO_4^{\bullet-}$) oxidation is a non-selective oxidation process, which results in the generation of more toxic intermediates in the systems of Co_{MC}-NC/PMS and Co_{NP}-NC. Further toxicity assessment also demonstrated that the reasonable regulation of degradation pathway could reduce the biotoxicity of the effluent (after reaction) to a certain extent. We believe that the degradation routes switched by active center size-dependent catalysts in Fenton-like reaction presented in this study is one example among many regulated strategies that can be further pursued. Particularly, we expect that this work can provide new insights into the regulation of reaction mechanisms and degradation routes in PMS-AOPs for wastewater treatment.

CRediT authorship contribution statement

Xinhao Wang: Conceptualization, Formal analysis, Investigation, Writing – original draft, Writing – review & editing. **Zhaokun Xiong:** Conceptualization, Data curation, Writing – review & editing, Project administration, Funding acquisition. **Hongle Shi:** Funding acquisition. **Zelin Wu:** Investigation, Formal analysis. **Bingkun Huang:** Methodology, Formal analysis. **Heng Zhang:** Formal analysis. **Peng Zhou:** Formal analysis. **Zhicheng Pan:** Validation. **Wen Liu:** Data curation, Formal analysis. **Bo Lai:** Validation, Conceptualization, Funding acquisition.

Declaration of Competing Interest

The authors declare that they have no known competing financial interests or personal relationships that could have appeared to influence the work reported in this paper.

Data availability

Data will be made available on request.

Acknowledgments

The authors would like to acknowledge the financial support from the National Natural Science Foundation of China (No. 52200105, 52070133), the National Key Research and Development Program of China (Grant No. 2021YFA1202500), Sichuan Program of Science and Technology (2023NSFSC0344, 2023JDZH0010) and China Postdoctoral Science Foundation (2022M710993).

Appendix A. Supporting information

Supplementary data associated with this article can be found in the online version at doi:10.1016/j.apcatb.2023.122569.

References

[1] L. Qiao, Y. Shi, Q.L. Cheng, B.T. Liu, J. Liu, The removal efficiencies and mechanism of aniline degradation by peroxydisulfate activated with magnetic Fe-Mn oxides composite, Water Reuse 11 (2021) 212–223.
[2] Z. Shen, H. Zhou, P. Zhou, H. Zhang, Z. Xiong, Y. Yu, G. Yao, B. Lai, Degradation of atrazine in water by Bi2MoO6 and visible light activated Fe(3+)/peroxymonosulfate coupling system, J. Hazard. Mater. 425 (2022), 127781.

[3] L. Jiao, H.L. Jiang, Metal-Organic-Framework-Based Single-Atom Catalysts for Energy Applications, Chem 5 (2019) 786–804.
[4] M.S. Cui, K.P. Cui, X.L. Liu, J.P. Shi, X. Chen, Y.H. Chen, Synergistic effect of mesoporous graphitic carbon nitride and peroxydisulfate in visible light-induced degradation of atenolol: A combined experimental and theoretical study, Chem. Eng. J. 412 (2021), 127979.
[5] K. Qian, H. Chen, W. Li, Z. Ao, Y.N. Wu, X. Guan, Single-Atom Fe Catalyst Outperforms Its Homogeneous Counterpart for Activating Peroxymonosulfate to Achieve Effective Degradation of Organic Contaminants, Environ. Sci. Technol. 55 (2021) 7034–7043.
[6] Y. Shang, X. Xu, B. Gao, S. Wang, X. Duan, Single-atom catalysis in advanced oxidation processes for environmental remediation, Chem. Soc. Rev. 50 (2021) 5281–5322.
[7] L. Wu, B. Li, Y. Li, X. Fan, F. Zhang, G. Zhang, Q. Xia, W. Peng, Preferential Growth of the Cobalt (200) Facet in Co@N–C for Enhanced Performance in a Fenton-like Reaction, ACS Catal. 11 (2021) 5532–5543.
[8] Y.F. Qi, J. Li, Y.Q. Zhang, Q. Cao, Y.M. Si, Z.R. Wu, M. Akram, X. Xu, Novel lignin-based single atom catalysts as peroxymonosulfate activator for pollutants degradation: Role of single cobalt and electron transfer pathway, Appl. Catal. B 286 (2021), 119910.
[9] L. Liu, Y. Li, W. Li, R. Zhong, Y. Lan, J. Guo, The efficient degradation of sulfisoxazole by singlet oxygen ((1)O2) derived from activated peroxymonosulfate (PMS) with Co3O4-SnO2/RSBC, Environ. Res. 187 (2020), 109665.
[10] Z.L. Wu, Y.P. Wang, Z.K. Xiong, Z.M. Ao, S.Y. Pu, G. Yao, B. Lai, Core-shell magnetic Fe3O4@Zn/Co-ZIFs to activate peroxymonosulfate for highly efficient degradation of carbamazepine, Appl. Catal. B 277 (2020), 119136.
[11] H.X. Yin, J. Li, H.D. Yan, H.Y. Cai, Y.J. Wan, G. Yao, Y. Guo, B. Lai, Activation of peroxymonosulfate by CuCo2O4 nano-particles towards long-lasting removal of atrazine, Water Reuse 11 (2021) 542–559.
[12] D. Rao, Y. Sun, B. Shao, J. Qiao, X. Guan, Activation of oxygen with sulfite for enhanced Removal of Mn(II): The involvement of SO4(*), Water Res. 157 (2019) 435–444.
[13] Y. Li, L. Guo, D. Huang, A. Jawad, Z. Chen, J. Yang, W. Liu, Y. Shen, M. Wang, G. Yin, Support-dependent active species formation for CuO catalysts: Leading to efficient pollutant degradation in alkaline conditions, J. Hazard. Mater. 328 (2017) 56–62.
[14] G.X. Huang, C.Y. Wang, C.W. Yang, P.C. Guo, H.Q. Yu, Degradation of Bisphenol A by Peroxymonosulfate Catalytically Activated with Mn1.8Fe1.2O4 Nanospheres: Synergism between Mn and Fe, Environ. Sci. Technol. 51 (2017) 12611–12618.
[15] X.G. Duan, H.Q. Sun, Z.P. Shao, S.B. Wang, Nonradical reactions in environmental remediation processes: Uncertainty and challenges, Appl. Catal. B 224 (2018) 973–982.
[16] X. Duan, H. Sun, Y. Wang, J. Kang, S. Wang, N-Doping-Induced Nonradical Reaction on Single-Walled Carbon Nanotubes for Catalytic Phenol Oxidation, ACS Catal. 5 (2014) 553–559.
[17] Y. Zhang, H.H. Pan, M. Murugananthan, P. Sun, D.D. Dionysiou, K.K. Zhang, A. Khan, Y.R. Zhang, Glucose and melamine derived nitrogen-doped carbonaceous catalyst for nonradical peroxymonosulfate activation, Carbon 156 (2020) 399–409.
[18] W.J. Ma, N. Wang, Y.A. Fan, T.Z. Tong, X.J. Han, Y.C. Du, Non-radical-dominated catalytic degradation of bisphenol A by ZIF-67 derived nitrogen-doped carbon nanotubes frameworks in the presence of peroxymonosulfate, Chem. Eng. J. 336 (2018) 721–731.
[19] X.G. Duan, Z.M. Ao, L. Zhou, H.Q. Sun, G.X. Wang, S.B. Wang, Occurrence of radical and nonradical pathways from carbocatalysts for aqueous and nonaqueous catalytic oxidation, Appl. Catal. B 188 (2016) 98–105.
[20] Y.Y. Ahn, E.T. Yun, J.W. Seo, C. Lee, S.H. Kim, J.H. Kim, J. Lee, Activation of Peroxymonosulfate by Surface-Loaded Noble Metal Nanoparticles for Oxidative Degradation of Organic Compounds, Environ. Sci. Technol. 50 (2016) 10187–10197.
[21] X.T. Li, J. Wang, X.G. Duan, Y. Li, X.B. Fan, G.L. Zhang, F.B. Zhang, W.C. Peng, Fine-Tuning Radical/Nonradical Pathways on Graphene by Porous Engineering and Doping Strategies, ACS Catal. 11 (2021) 4848–4861.
[22] A. Jawad, K. Zhan, H. Wang, A. Shahzad, Z. Zeng, J. Wang, X. Zhou, H. Ullah, Z. Chen, Z. Chen, Tuning of Persulfate Activation from a Free Radical to a Nonradical Pathway through the Incorporation of Non-Redox Magnesium Oxide, Environ. Sci. Technol. 54 (2020) 2476–2488.
[23] N. Li, R. Li, X. Duan, B. Yan, W. Liu, Z. Cheng, G. Chen, L. Hou, S. Wang, Correlation of Active Sites to Generated Reactive Species and Degradation Routes of Organics in Peroxymonosulfate Activation by Co-Loaded Carbon, Environ. Sci. Technol. 55 (2021) 16163–16174.
[24] Z.K. Xiong, Y.N. Jiang, Z.L. Wu, G. Yao, B. Lai, Synthesis strategies and emerging mechanisms of metal-organic frameworks for sulfate radical-based advanced oxidation process: A review, Chem. Eng. J. 421 (2021), 127863.
[25] H. Zhang, S. Duan, P.M. Radjenovic, Z.Q. Tian, J.F. Li, Core-Shell Nanostructure-Enhanced Raman Spectroscopy for Surface Catalysis, Acc. Chem. Res. 53 (2020) 729–739.
[26] Y. Wang, J. Le Roux, T. Zhang, J.P. Croue, Formation of brominated disinfection byproducts from natural organic matter isolates and model compounds in a sulfate radical-based oxidation process, Environ. Sci. Technol. 48 (2014) 14534–14542.
[27] M.J. Frisch, G.W. Trucks, H.B. Schlegel, G.E. Scuseria, M.A. Robb, J.R. Cheeseman, G. Scalmani, V. Barone, G.A. Petersson, H. Nakatsuji, X. Li, M. Caricato, A. V. Marenich, J. Bloino, B.G. Janesko, R. Gomperts, B. Mennucci, H.P. Hratchian, J. V. Ortiz, A.F. Izmaylov, J.L. Sonnenberg, Williams, F. Ding, F. Lipparini, F. Egidi, J. Goings, B. Peng, A. Petrone, T. Henderson, D. Ranasinghe, V.G. Zakrzewski, J. Gao, N. Rega, G. Zheng, W. Liang, M. Hada, M. Ehara, K. Toyota, R. Fukuda, J. Hasegawa, M. Ishida, T. Nakajima, Y. Honda, O. Kitao, H. Nakai, T. Vreven, K. Throssell, J.A. Montgomery Jr, J.E. Peralta, F. Ogliaro, M.J. Bearpark, J.J. Heyd, E.N. Brothers, K.N. Kudin, V.N. Staroverov, T.A. Keith, R. Kobayashi, J. Normand, K. Raghavachari, A.P. Rendell, J.C. Burant, S.S. Iyengar, J. Tomasi, M. Cossi, J. M. Millam, M. Klene, C. Adamo, R. Cammi, J.W. Ochterski, R.L. Martin, K. Morokuma, O. Farkas, J.B. Foresman, D.J. Fox, Gaussian 16 Rev. C.01, Wallingford, CT,, 2016.
[28] A.D. Becke, Density-functional exchange-energy approximation with correct asymptotic behavior, Phys. Rev. A Gen. Phys. 38 (1988) 3098–3100.
[29] S. Grimme, J. Antony, S. Ehrlich, H. Krieg, A consistent and accurate ab initio parametrization of density functional dispersion correction (DFT-D) for the 94 elements H-Pu, J. Chem. Phys. 132 (2010), 154104.
[30] J. Tomasi, B. Mennucci, R. Cammi, Quantum mechanical continuum solvation models, Chem. Rev. 105 (2005) 2999–3093.
[31] R.G. Parr, W. Yang, Density functional approach to the frontier-electron theory of chemical reactivity, J. Am. Chem. Soc. 106 (2002) 4049–4050.
[32] F.L. Hirshfeld, Bonded-atom fragments for describing molecular charge densities, Theor. Chim. Acta 44 (1977) 129–138.
[33] T. Lu, F. Chen, Multiwfn: a multifunctional wavefunction analyzer, J. Comput. Chem. 33 (2012) 580–592.
[34] Y.N. Jiang, Z.K. Xiong, J.B. Huang, F. Yan, G. Yao, B. Lai, Effective E. coli inactivation of core-shell ZnO@ZIF-8 photocatalysis under visible light synergize with peroxymonosulfate: Efficiency and mechanism, Chin. Chem. Lett. 33 (2022) 415–423.
[35] X. Li, X. Huang, S. Xi, S. Miao, J. Ding, W. Cai, S. Liu, X. Yang, H. Yang, J. Gao, J. Wang, Y. Huang, T. Zhang, B. Liu, Single Cobalt Atoms Anchored on Porous N-Doped Graphene with Dual Reaction Sites for Efficient Fenton-like Catalysis, J. Am. Chem. Soc. 140 (2018) 12469–12475.
[36] Y. Shang, X. Duan, S. Wang, Q. Yue, B. Gao, X. Xu, Carbon-based single atom catalyst: Synthesis, characterization, DFT calculations, Chin. Chem. Lett. 33 (2022) 663–673.
[37] B. Huang, Z. Wu, H. Zhou, J. Li, C. Zhou, Z. Xiong, Z. Pan, G. Yao, B. Lai, Recent advances in single-atom catalysts for advanced oxidation processes in water purification, J. Hazard. Mater. 412 (2021), 125253.
[38] S. Dilpazir, H.Y. He, Z.H. Li, M. Wang, P.L. Lu, R.J. Liu, Z.J. Xie, D.L. Gao, G. J. Zhang, Cobalt Single Atoms Immobilized N-Doped Carbon Nanotubes for Enhanced Bifunctional Catalysis toward Oxygen Reduction and Oxygen Evolution Reactions, ACS Appl. Energy Mater. 1 (2018) 3283–3291.
[39] Z. Wu, Z. Xiong, R. Liu, C. He, Y. Liu, Z. Pan, G. Yao, B. Lai, Pivotal roles of N-doped carbon shell and hollow structure in nanoreactor with spatial confined Co species in peroxymonosulfate activation: Obstructing metal leaching and enhancing catalytic stability, J. Hazard. Mater. 427 (2022), 128204.
[40] Y. Liu, Z. Zhao, W. Wei, X. Jin, G. Wang, K. Li, Y. Lin, Single-Atom Fe-N4 on a Carbon Substrate for Nitrogen Reduction Reaction, ACS Appl. Nano Mater. 4 (2021) 13001–13009.
[41] J. Miao, Y. Zhu, J. Lang, J. Zhang, S. Cheng, B. Zhou, L. Zhang, P.J.J. Alvarez, M. Long, Spin-State-Dependent Peroxymonosulfate Activation of Single-Atom M–N Moieties via a Radical-Free Pathway, ACS Catal. 11 (2021) 9569–9577.
[42] W. Xie, Y. Song, S. Li, J. Li, Y. Yang, W. Liu, M. Shao, M. Wei, Single-Atomic-Co Electrocatalysts with Self-Supported Architecture toward Oxygen-Involved Reaction, Adv. Funct. Mater. 29 (2019) 1906477.
[43] Z. Guo, Y. Xie, J. Xiao, Z.J. Zhao, Y. Wang, Z. Xu, Y. Zhang, L. Yin, H. Cao, J. Gong, Single-Atom Mn-N4 Site-Catalyzed Peroxone Reaction for the Efficient Production of Hydroxyl Radicals in an Acidic Solution, J. Am. Chem. Soc. 141 (2019) 12005–12010.
[44] Q. Zhang, I. Lee, J.B. Joo, F. Zaera, Y. Yin, Core-shell nanostructured catalysts, Acc. Chem. Res. 46 (2013) 1816–1824.
[45] X.G. Duan, H.Q. Sun, Z.M. Ao, L. Zhou, G.X. Wang, S.B. Wang, Unveiling the active sites of graphene-catalyzed peroxymonosulfate activation, Carbon 107 (2016) 371–378.
[46] L. Li, Z. Yin, M. Cheng, L. Qin, S. Liu, H. Yi, M. Zhang, Y. Fu, X. Yang, X. Zhou, G. Zeng, C. Lai, Insights into reactive species generation and organics selective degradation in Fe-based heterogeneous Fenton-like systems: A critical review, Chem. Eng. J. 454 (2023), 140126.
[47] L. Li, M. Cheng, L. Qin, E. Almatrafi, X. Yang, L. Yang, C. Tang, S. Liu, H. Yi, M. Zhang, Y. Fu, X. Zhou, F. Xu, G. Zeng, C. Lai, Enhancing hydrogen peroxide activation of CuCo layered double hydroxide by compositing with biochar: Performance and mechanism, Sci. Total Environ. 828 (2022), 154188.
[48] C. Lai, D. Ma, H. Yi, M. Zhang, F. Xu, X. Huo, H. Ye, L. Li, L. Yang, L. Tang, M. Yan, Functional partition of Fe and Ti co-doped g-C3N4 for photo-Fenton degradation of oxytetracycline: Performance, mechanism, and DFT study, Sep. Purif. Technol. 306 (2023), 122546.
[49] W. Ren, C. Cheng, P. Shao, X. Luo, H. Zhang, S. Wang, X. Duan, Origins of electron-transfer regime in persulfate-based nonradical oxidation processes, Environ. Sci. Technol. 56 (2022) 78–97.
[50] Z.H. Xie, C.S. He, H.Y. Zhou, L.L. Li, Y. Liu, Y. Du, W. Liu, Y. Mu, B. Lai, Effects of Molecular Structure on Organic Contaminants' Degradation Efficiency and Dominant ROS in the Advanced Oxidation Process with Multiple ROS, Environ. Sci. Technol. 56 (2022) 8784–8795.
[51] M. Yang, Z. Hou, X. Zhang, B. Gao, Y. Li, Y. Shang, Q. Yue, X. Duan, X. Xu, Unveiling the Origins of Selective Oxidation in Single-Atom Catalysis via Co-N(4)-C Intensified Radical and Nonradical Pathways, Environ. Sci. Technol. 56 (2022) 11635–11645.
[52] Y. Hong, H. Zhou, Z. Xiong, Y. Liu, G. Yao, B. Lai, Heterogeneous activation of peroxymonosulfate by CoMgFe-LDO for degradation of carbamazepine: Efficiency, mechanism and degradation pathways, Chem. Eng. J. 391 (2020), 123604.

[53] J.J. You, C.Y. Zhang, Z.L. Wu, Z.M. Ao, W.Y. Sun, Z.K. Xiong, S.J. Su, G. Yao, B. Lai, N-doped graphite encapsulated metal nanoparticles catalyst for removal of Bisphenol A via activation of peroxymonosulfate: A singlet oxygen-dominated oxidation process, Chem. Eng. J. 415 (2021), 128890.
[54] W. Wang, H. Yu, K. Li, F. Lin, C. Huang, B. Yan, Z. Cheng, X. Li, G. Chen, L.A. Hou, Insoluble matrix proteins from shell waste for synthesis of visible-light response photocatalyst to mineralize indoor gaseous formaldehyde, J. Hazard. Mater. 415 (2021), 125649.
[55] M.J. Xu, J. Li, Y. Yan, X.G. Zhao, J.F. Yan, Y.H. Zhang, B. Lai, X. Chen, L.P. Song, Catalytic degradation of sulfamethoxazole through peroxymonosulfate activated with expanded graphite loaded CoFe2O4 particles, Chem. Eng. J. 369 (2019) 403–413.
[56] K. Zhu, H. Jia, Y. Sun, Y. Dai, C. Zhang, X. Guo, T. Wang, L. Zhu, Long-term phototransformation of microplastics under simulated sunlight irradiation in aquatic environments: Roles of reactive oxygen species, Water Res. 173 (2020), 115564.
[57] M. Zhang, R. Luo, C. Wang, W. Zhang, X. Yan, X. Sun, L. Wang, J. Li, Confined pyrolysis of metal–organic frameworks to N-doped hierarchical carbon for non-radical dominated advanced oxidation processes, J. Mater. Chem. A 7 (2019) 12547–12555.
[58] X. Li, J. Liu, A.I. Rykov, H. Han, C. Jin, X. Liu, J. Wang, Excellent photo-Fenton catalysts of Fe–Co Prussian blue analogues and their reaction mechanism study, Appl. Catal. B 179 (2015) 196–205.
[59] Y. Gao, T. Wu, C. Yang, C. Ma, Z. Zhao, Z. Wu, S. Cao, W. Geng, Y. Wang, Y. Yao, Y. Zhang, C. Cheng, Activity Trends and Mechanisms in Peroxymonosulfate-Assisted Catalytic Production of Singlet Oxygen over Atomic Metal-N-C Catalysts, Angew. Chem. Int. Ed. Engl. 60 (2021) 22513–22521.
[60] R.L. Yin, Y.X. Chen, J.Y. Hu, G. Lu, L.X. Zeng, W.Y. Choi, M.S. Zhu, Complexes of Fe (III)-organic pollutants that directly activate Fenton-like processes under visible light, Appl. Catal. B 283 (2021), 119663.
[61] G. Piccirillo, M. Moreira-Santos, M. Valega, M.E.S. Eusebio, A.M.S. Silva, R. Ribeiro, H. Freitas, M.M. Pereira, M.J.F. Calvete, Supported metalloporphyrins as reusable catalysts for the degradation of antibiotics: Synthesis, characterization, activity and ecotoxicity studies, Appl. Catal. B 282 (2021), 119556.
[62] Y. Zong, X. Guan, J. Xu, Y. Feng, Y. Mao, L. Xu, H. Chu, D. Wu, Unraveling the Overlooked Involvement of High-Valent Cobalt-Oxo Species Generated from the Cobalt(II)-Activated Peroxymonosulfate Process, Environ. Sci. Technol. 54 (2020) 16231–16239.
[63] J. Wang, X. Duan, J. Gao, Y. Shen, X. Feng, Z. Yu, X. Tan, S. Liu, S. Wang, Roles of structure defect, oxygen groups and heteroatom doping on carbon in nonradical oxidation of water contaminants, Water Res. 185 (2020), 116244.
[64] H. Zhou, L. Lai, Y. Wan, Y. He, G. Yao, B. Lai, Molybdenum disulfide (MoS2): A versatile activator of both peroxymonosulfate and persulfate for the degradation of carbamazepine, Chem. Eng. J. 384 (2020).
[65] J. Peng, P. Zhou, H. Zhou, W. Liu, H. Zhang, C. Zhou, L. Lai, Z. Ao, S. Su, B. Lai, Insights into the Electron-Transfer Mechanism of Permanganate Activation by Graphite for Enhanced Oxidation of Sulfamethoxazole, Environ. Sci. Technol. 55 (2021) 9189–9198.
[66] J.Y. Yao, X.L. Zeng, Z.Y. Wang, Enhanced degradation performance of sulfisoxazole using peroxymonosulfate activated by copper-cobalt oxides in aqueous solution: Kinetic study and products identification, Chem. Eng. J. 330 (2017) 345–354.
[67] Y.L. Song, S.S. Gao, J.Y. Tian, H.Z. Zhang, Construction of Ag/g-C3N4 composites with uniform-sized Ag nanoparticles and the application for sulfisoxazole degradation in the presence of visible radiation, J. Environ. Chem. Eng. 8 (2020), 104390.
[68] L. Ge, P. Zhang, C. Halsall, Y. Li, C.E. Chen, J. Li, H. Sun, Z. Yao, The importance of reactive oxygen species on the aqueous phototransformation of sulfonamide antibiotics: kinetics, pathways, and comparisons with direct photolysis, Water Res. 149 (2019) 243–250.
[69] X. Long, H. Shi, R. Huang, L. Gu, Y. Liu, C.-s He, Y. Du, Z. Xiong, W. Liu, B. Lai, Identifying the evolution of primary oxidation mechanisms and pollutant degradation routes in the electro-cocatalytic Fenton-like systems, J. Hazard. Mater. 445 (2023), 130577.
[70] Y. Yu, Z. Xiong, B. Huang, X. Wang, Y. Du, C. He, Y. Liu, G. Yao, B. Lai, Synchronous removal of pharmaceutical contaminants and inactivation of pathogenic microorganisms in real hospital wastewater by electro-peroxone process, Environ. Int. 168 (2022), 107453.
[71] J. Fu, C.-H. Huang, C. Dang, Q. Wang, A review on treatment of disinfection byproduct precursors by biological activated carbon process, Chin. Chem. Lett. 33 (2022) 4495–4504.
[72] T. Wang, J. Zhou, W. Wang, Y. Zhu, J. Niu, Ag-single atoms modified S1.66-N1.91/TiO2-x for photocatalytic activation of peroxymonosulfate for bisphenol A degradation, Chin. Chem. Lett. 33 (2022) 2121–2124.